Article

Development of a large-bore plasma window with an indirectly heated hollow cathode

K. Yamasaki,[1] M. Sumino,[1] Y. Sunada,[1] O. Yanagi,[1] K. Okuda,[1] J. Kono,[1] A. Saito,[1] D. Mori,[1] K. Tomita,[2] Y. Pan,[2] N. Tamura,[3] C. Suzuki,[3] H. Okuno,[4] F. Guo,[1] and S. Namba[1]

[1)] *Graduate School of Advanced Science and Engineering, Hiroshima University, 1-4-1, Kagamiyama, Higashihiroshima, Hiroshima 739-8527, Japan*

[2)] *Division of Quantum Science and Engineering, Graduate School of Engineering, Hokkaido University, Kita 13, Nishi 8, Kita-Ku, Sapporo, Hokkaido 060-8628, Japan*

[3)] *Department of Research, National Institute for Fusion Science, 322-6 Oroshi-cyo, Toki, Gifu 509-5292, Japan*

[4)] *Nishina Center for Accelerator-Based Science, RIKEN, Wako, Saitama 351-0198, Japan*

(*Electronic mail: kotaro-yamasaki@hiroshima-u.ac.jp)

(Dated: 8 August 2023)

For plasma window (PW) applications, we developed the cascade arc discharge device with an indirectly heated hollow cathode. The 8-mm channel diameter hollow cathode made of a lanthanum hexaboride (LaB_6) was heated by the C/C composite heater surrounding the cathode to increase the thermionic electron emission. The PW developed successfully separated 2.4 kPa and 16 Pa, and the pressure separation capability was sustained for over 1 hour. H-β Stark broadening measurement and the Thomson scattering measurement showed that the electron density and temperature inside the channel reached 10^{19}-10^{20} m^{-3} and 2.0 eV, respectively. The power balance analysis on the electron thermal energy revealed that the neutral density and temperature inside the channel were as high as 10^{23} m^{-3} and 4000 K, respectively. The relation between the pressure separation capability and the neutral temperature showed that the flow inside the channel of the PW had the molecular flow feature. The SEM-EDX analysis on the LaB_6 cathode showed that the boron diffused to the molybdenum (Mo) shaft during plasma operation, which supported the LaB_6 cathode. Mo shaft became brittle after more than 50 hours of operation, exhibiting the necessity of buffer material between the LaB_6 cathode and Mo shaft for long-duration operation.

I. INTRODUCTION

The plasma window (PW) is a plasma application technique that separates a high-pressure (10-100 kPa) and vacuum (1 Pa) environment without using solid materials such as glass and stainless steel. The plasma inside the channel of the PW heats the neutral gas and increases the gas temperature, reducing the flow conductance. The flow inside the channel is considerably suppressed due to the decrease in the conductance, and the pressure difference between the gas inlet and outlet of the PW is kept to be substantially high[1–3]. These features enable the PW to transmit the soft-X rays, electron, and ion beams into the atmospheric pressure side without drastic beam attenuation/scattering[1,4,5]. This prominent feature of PW is expected to pave the way for the new application of quantum beam science.

The PW was invented by Ady Hershcovitch in 1995, achieving the separation of atmospheric pressure and 533 Pa through the channel with inner diameter and length of 2.36 mm and 60 mm, respectively[4]. The PW successfully demonstrated the electron beam welding in the atmospheric pressure environment. Since then, various attempts were made to transmit the beams and x-rays to the atmospheric environment. Pinkoski and coworkers realized soft X-ray transmission through the PW[5]. In this case, the PW demonstrated the transmission of 9.6 keV X-ray through the channel with 2 mm diameter and 40 mm length while maintaining the pressure difference of 1.2×10^{-2} bar and 2.6×10^{-4} bar, which could not be observed when the PW was turned off. Detailed analysis on the performance of the PW have been done by W. A. Vijvers *et al.* , experimentally and theoretically elucidating the mechanism of the pressure separation capability of PWs whose channel diameter ranged from 4 mm to 8 mm [6]. Huang *et al.* analyzed the pressure separation capability using detailed spectroscopic techniques[2]. Recently, the PW with larger inner diameter and rectangular cross section have been developed for ion beam application[3,7] and for an advanced tokamak divertor scenario[8].

One of the applications of the PW under consideration is an alternative differential pumping method for helium (He) gas cell stripper in the heavy ion beam accelerators at RIKEN[9]. The production of heavy ion beams, such as gold and uranium ions, has extensively been studied for rare isotope research[10]. The charge state of the heavy ions must be sufficiently high at the initial stage of the accelerators to achieve higher beam energy. The conventional method for realizing the high charge state of the heavy ions employs the carbon foils of a few $\mu g/cm^2$ to several tens of mg/cm^2 [9]. However, the lifetime of the foil is limited to about half a day due to the damage and thinning of the foil itself[9,11]. In addition, great care has to be taken to the uniformity of the foil thickness to reduce the energy spread of the beam. In view of the drawbacks of the carbon foil charge strippers, the He gas cell stripper has been studied to overcome these problems in terms of lifetime and uniformity[11]. The He gas stripper consists of a 50-cm long, 7 kPa gas cell and five differential pumping systems at both sides of the gas cell. This enables the heavy ion beam to interact with He gas, resulting in the production of even higher charged ions, while the beamlines is maintained at low vacuum pressure[2]. Since the helium gas stripper system requires

22 pumps and 200 L/min of He gas flow to keep the pressures of the gas cell (7 kPa) and beam transport line (10^{-6} Pa)[12], some differential pumps with lower conductance are needed to reduce the size of the system, the amount of He gas, and operation cost. A PW with a large bore has been developed to realize a lower conductance differential pumping system for application to the He gas stripper[7]. Ikoma *et al.*[7] successfully separated 20 kPa and 0.2 Pa using the PW, whose bore is 10 mm in diameter under the gas flow rate of 20 L/min. However, the PWs previously developed have used needle-shaped cathodes, which often suffers from heat load and wear out after long hours of discharge[13]. The cathode structure, therefore, must be improved so as for PW to operate sufficiently long duration.

A hollow cathode[14] can be one of the candidates for the cathode of the PWs which reduce the heat load at a unit surface area. A hollow cathode is a cylinder-shaped electrode used for various purposes, such as research on basic plasma physics[15], development of ion lasers[16,17], thrusters for spacecraft[18], and modification of the material surface[19]. The hollow cathode's primary attribute is its internal plasma column (IPC), a high-density and high-temperature plasma generated within the hollow electrode[14]. Since the hollow cathode discharge starts from the inner surface of the electrode, the effective surface area of the cathode increases, resulting in the reduction of heat load at a unit area and enhancement of the lifetime of the cathode materials. Moreover, the IPC is suitable for the PW application, because the high-density and high-temperature plasma heats the inlet gas and may contributes to the increase in the pressure separation owing to the increased gas viscosity.

Typical hollow cathodes are operated at a low-pressure environment in the range of 10^{-3}-1 Pa, and previous studies have shown that the IPC cannot be formed under a high-pressure environment, namely 10 kPa [14]. However, it has also been revealed that the IPC can be created in a high-pressure environment by heating the hollow cathode[14]. These results suggest that the PW aiming at operating in a high-pressure environment for a sufficiently long time requires the auxiliary heating system for the cathode material, similar to the hollow cathodes installed in hall thrusters[18,20,21] and high-density plasma source[22]. In this study, we developed an 8 mm inner-diameter PW apparatus equipped with a hollow shaped cathode made of thermionic material (LaB_6) heated indirectly.

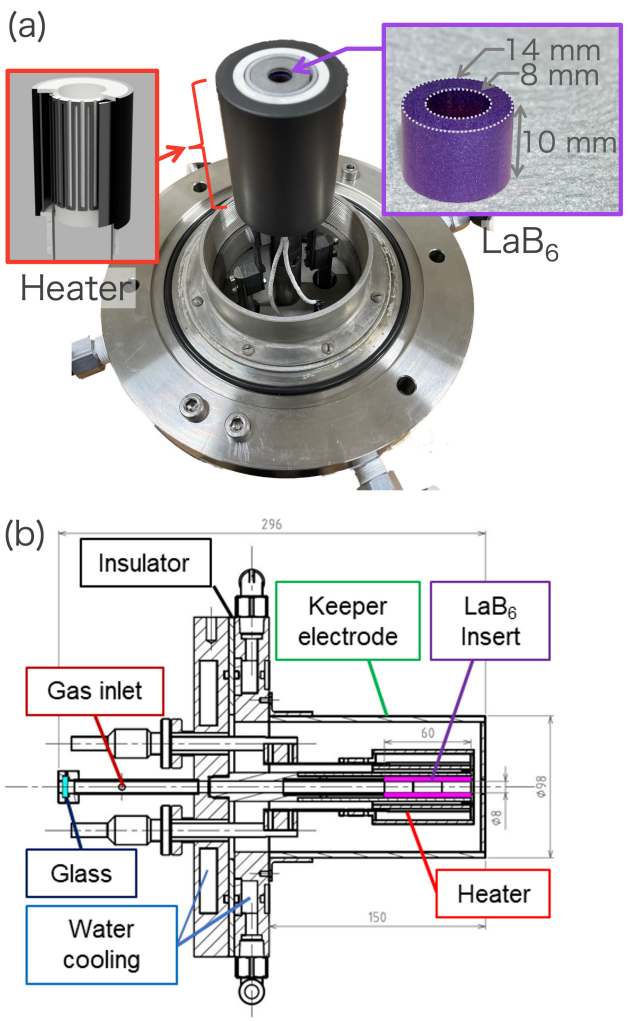

FIG. 1. (a)Photo of the developed hollow cathode for a large bore plasma window. (b) Schematic diagram of the hollow cathode.

Parameters	Values or names
Working gas	helium
Gas flow	0.05-0.6 L/min
Axial magnetic field at channel	~98 mT
Discharge current	~100 A
Discharge voltage	~200 V
LaB_6 cathode temperature at work	1700 °C

TABLE I. Summary of the discharge parameters of the plasma window.

II. EXPERIMENTAL SETUP

The schematic diagram of the PW is shown in Fig. 1. The cathode component consisted of the cylindrical thermionic material, a lanthanum hexaboride (LaB_6 , work function: 2.66 eV [23]), a heater and a keeper electrode, as shown in Fig. 1(a) and (b). The length, outer and inner diameters of the LaB_6 cylinder were 10 mm, 14 mm, and 8 mm, respectively, and six piece of these were inserted into the molybdenum (Mo) shaft, whose length, outer and inner diameter were 120 mm, 20 mm and 15 mm, respectively, resulting in the inner surface area of 150 mm^2, 6.5 times larger than that of the needle-shaped electrode previously used for the PW cathode[3]. The large internal surface area facilitated the thermionic electron current up to 200 A when the LaB_6 was heated to 1700 °C. The C/C (Carbon Fiber Reinforced Carbon) composite heater surrounding the Mo shaft (see Figure 1(b)) heated the LaB_6 cathode. The heater's power supply, whose AC output voltage and current reached up to 45 V and 40 A, respectively, was controlled based on PID control following the input from the C-type thermocouple to maintain the temperature of the LaB_6

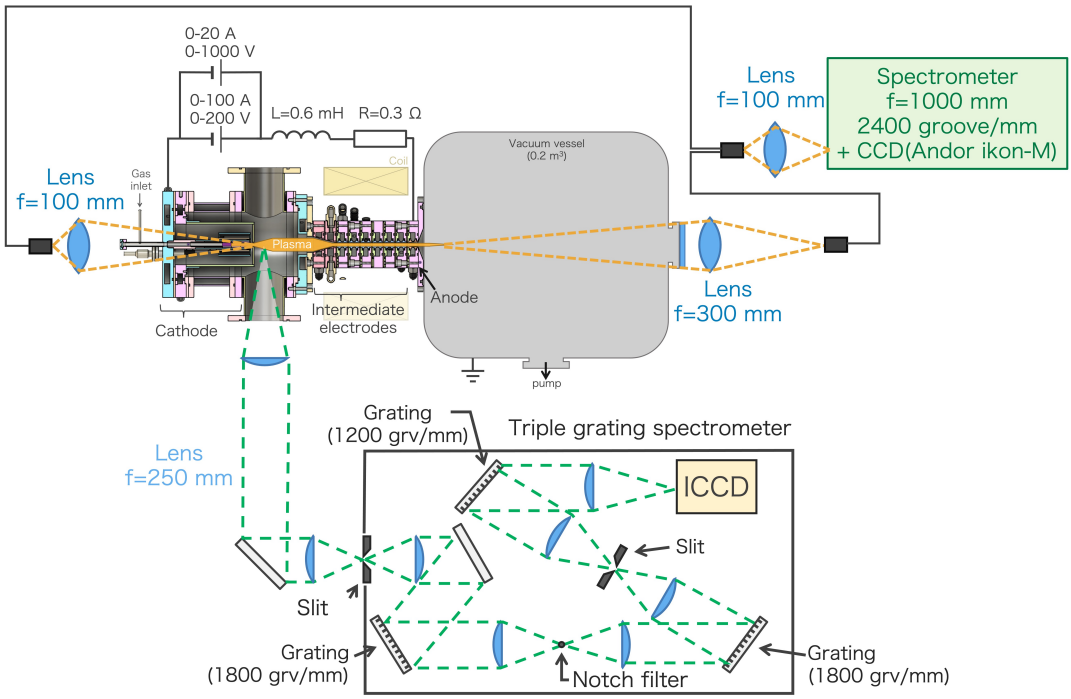

FIG. 2. Schematic diagram of the plasma window, vacuum vessel, and discharge circuit, together with that of the H-β Stark broadening and the Thomson scattering measurement system. The laser path of the Nd:YAG laser used for the Thomson scattering measurement is not shown. The lens used in the triple grating spectrometer are plano-convex lens with a focal length of 250 mm.

constant during the discharge. The heater and Mo shaft were electrically insulated by a cylinder made of boron nitride. The keeper electrode was spaced 5 mm from the tip of the Mo shaft. The intermediate electrode was spaced 97 mm from the keeper electrode to perform Thomson scattering measurement just at the downstream of the cathode exit, as shown in Fig. 2.

The channel of the anode and the intermediate electrodes, except those with tapered channels, were made of Mo, as shown in Fig. 3. The inner diameter of the intermediate electrodes was 8 mm, while that of the anode had a diverging shape from 8 mm to 10 mm. The Mo part was cooled by water. The anode and the intermediate electrodes were insulated by Teflon disks with 3-mm thick to have the intermediate electrodes to be electrically floated. The PW was connected to the vacuum vessel (plasma expansion chamber), whose inner volume was 0.2 m^3 (see Fig. 2). The vacuum vessel was evacuated by two sets of rotary pumps (Edwards E2M80) and mechanical booster pumps (Edwards EH500A), realizing the pumping speed of 400 m^3/h for each group. The solenoid coil was placed coaxially with the channel to produce a magnetic field strength of 98 mT at the center of the intermediate electrodes (see Fig. 2). The He gas was fed from the gas inlet tube installed in the cathode flange (see Fig. 1(b) and Fig. 2) using a mass flow controller (ATOVAC AFC500) to control the gas flow rate up to 2.0 L/min. Two different types of power supplies are connected to the anode and cathode in parallel; one can supply up to 1 kV and 20 A, and the other can supply up to 200 V and 100A for the ignition and sustainment of the discharge, respectively. The operation ranges of the controllable

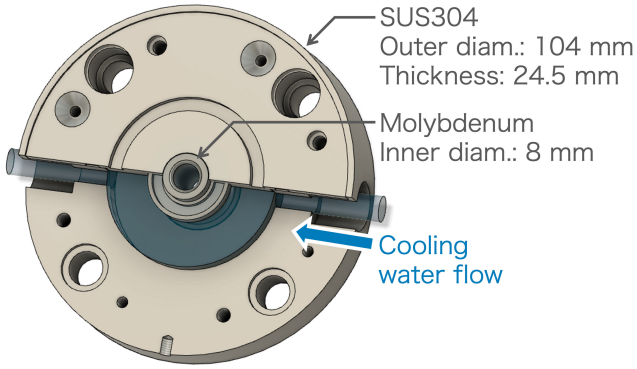

FIG. 3. Schematic diagram of the intermediate electrode.

parameters are listed in TABLE I.

The H-β (486.1 nm) Stark broadening and Thomson scattering measurements were performed to determine the electron density and temperature. A schematic diagram of the two measurement systems is shown in Fig. 2. Both H-β emissions at the cathode and anode exits originating from the impurity hydrogen were collected by the lens and fed to the optical fiber connected to the spectrometer (Jobin Yvon HR-1000), whose focal length and the number of grooves was 1000 mm and 2400 grooves/mm, respectively. The CCD camera (ANDOR ikon-M, DU934P-BU2-SE, 1024×1024 pix, 13 μm pitch) was connected to the spectrometer, enabling the spectroscopic ob-

servation with a reciprocal linear dispersion of 0.0036 nm/pix (0.27 nm/mm) and instrumental width of 12 pm (Gaussian profile, full width at half maximum) when the slit width was set to 30 μm. The focal lengths of the lens for collecting H-β emission were f=100 mm and f=300 mm for the cathode and anode observations, respectively. Therefore, the density evaluated by the H-β Stark broadening represented the average values within a few millimeters from the focus. The Stark broadening width was obtained by fitting the Voigt function to the H-β spectrum, and subsequently the electron density was calculated using the relation between electron density and Stark width[24].

Schematic diagram of the Thomson scattering measurement system is shown in Fig. 2. The frequency-doubled Nd:YAG laser (532 nm, 200 mJ, 8 ns) was injected from the window at the end of the vacuum vessel and focused at the cathode exit using the lens with a focal length of 1500 mm. The 90° scattered light at 2 cm downstream from the keeper was collected in the direction normal to the incident beam. Subsequently, the scattered signal was fed to a triple grating spectrometer using a pair of plano-convex lenses with a focal length of 250 mm. The triple grating spectrometer was composed of three gratings and a notch filter. The light passing through the first slit was dispersed by the first grating (1800 groove/mm) and inversely dispersed by the second grating (1800 groove/mm) to eliminate the stray light from the out of the region of interest[25–28]. The notch filter between the two gratings eliminated the spectrum attributed to 532-nm stray light to improve the signal-to-noise ratio. The spectrum dispersed by the third grating (1200 groove/mm) was observed by an ICCD camera (Princeton Instruments PI-MAX1KUV-18-43-U, 1024×1024 pix, 13 μm pitch). The calibration of the density and the reciprocal linear dispersion was performed by the Rayleigh and Raman spectrum from N_2 molecules, respectively. The Raman spectrum observation confirmed that the reciprocal linear dispersion was 0.039 nm/pixel (3.0 nm/mm) and that the notch filter eliminated the light within 532 $\pm$ 1.6 nm, indicating that the notch filter enabled us to measure even cold temperature plasma as low as 0.3 eV.

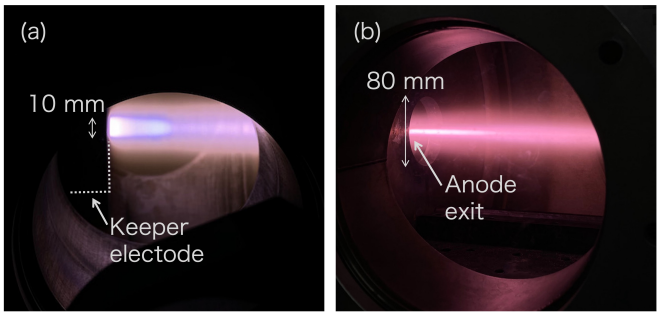

FIG. 4. Photo of the plasma produced by the cascade arc discharge with indirectly heated hollow cathode (a) viewed from the side of the cathode and (b) from the window at the vacuum vessel. The discharge was initiated with a gas flow rate of 0.07 L/min and a discharge current of 30 A.

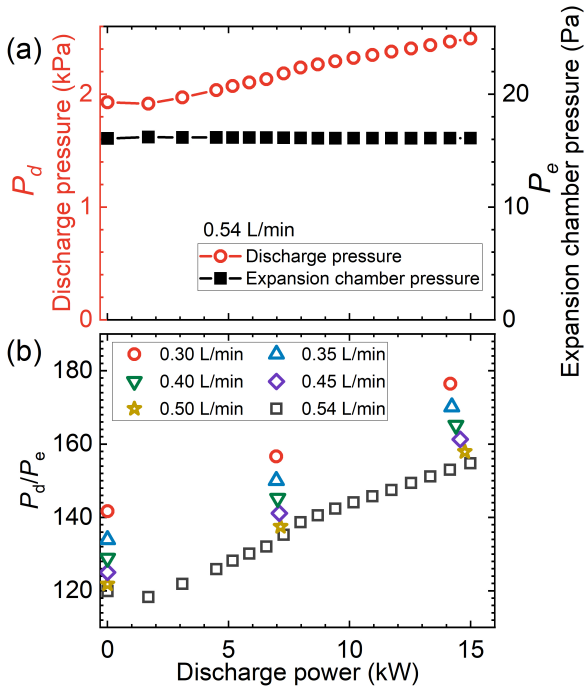

FIG. 5. (a) The dependence of the pressure at the cathode (P_d) and vacuum vessel (P_e) on the discharge power under 0.54 L/min and (b) the dependence of the pressure ratio on the discharge power.

III. RESULTS AND DISCUSSION

A. Pressure separation capability

The cascade arc discharge was successfully initiated just after applying 1 kV between the anode and cathode under the condition of a gas flow rate of 1.0 L/min and magnetic field strength of 98 mT when the temperature of the LaB_6 hollow cathode was kept at 1700 °C by using the heater. Since the previous PW with a self-heating hollow cathode[29] could not initiate the discharge before the temperature of the LaB_6 reached sufficiently high, the heater in PW developed contributed to the stable initiation of the arc discharge. The photograph of the cascade arc plasma produced by the PW suggests that the radius of the plasma is almost constant from the cathode exit to the intermediate electrode (see Fig. 4 (a)), while the emission intensity starts decreasing about 5 cm downstream from the keeper. The bright and dark emission regions are often observed at the anode exit of the arc jet plasma, because the expansion and compression wave were formed repeatedly under-expanded supersonic flow[30]. Therefore, the variation of the emission intensity along the plasma column may represent the non-uniformity of the plasma density along the channel. This feature can be observed in various discharge conditions within the gas flow rate of 0.07-0.28 L/min and discharge current of 30-100 A.

The dependence of the pressure at the gas inlet (termed as discharge pressure or P_d) and at the vacuum vessel (termed as expansion chamber pressure or P_e) on the discharge power is

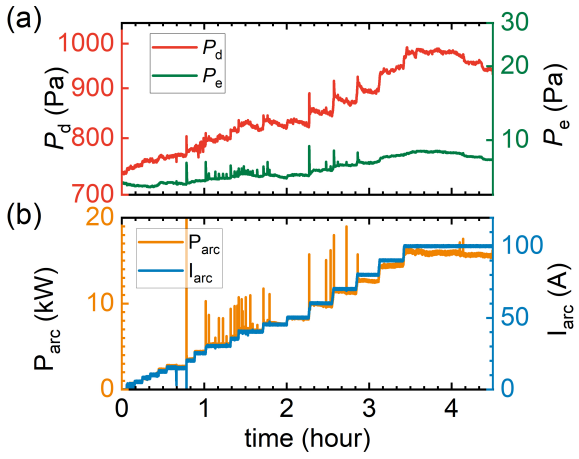

FIG. 6. The temporal evolution of (a) the pressure at the gas inlet (P_d) and the vacuum chamber (P_e) and (b) the discharge power (P_{arc}) and current (I_{arc}).

shown in Fig. 5 (a) with a gas flow rate of 0.54 L/min. The discharge pressure monotonically increased with the discharge power, while the expansion chamber pressure is kept constant. At a discharge power of 15 kW, the discharge pressure reaches 2.4 kPa while the expansion chamber pressure is maintained at 16 Pa. The increase in the discharge pressure was observed for various gas flow rate conditions. Figure 5 (b) shows the ratio of the discharge pressure to the expansion chamber pressure. Since the expansion chamber pressure is not changed with the discharge power, the increase in the pressure ratio suggests that the pressure separation capability increases with the discharge power. The time evolutions of P_d, P_e, discharge current and power are shown in Fig. 6 (a) and (b) with the gas flow rate of 0.07 L/min. The PW successfully maintains the pressure difference of about 1 kPa for more than an hour, showing that the PW equipped with the indirectly-heated hollow cathode is a promising candidate for a vacuum interface application.

B. Discharge Characteristics

The electrode position, the heat load and electric potential at each electrode are shown in Fig. 7 (a), (b) and (c), respectively. The heat load on each electrode are calculated from the temperature and the flow rate of the cooling water. Although the heat load is monotonically increased with the discharge current, the potential profile is kept constant. The potential gradient is almost constant within the intermediate electrode, while at the anode position it is steeper, implying the existence of space charge layer which is often observed at the anode surface of arc discharge[31]. The heat load of the intermediate electrode is decreased with getting close to the anode, while the heat load on the anode was significantly high compared to the neighbouring intermediate electrode. The Joule heating inside the anode electrode, no more than 0.1 kW calculated from the resistivity between anode channel and vacuum vessel, is one

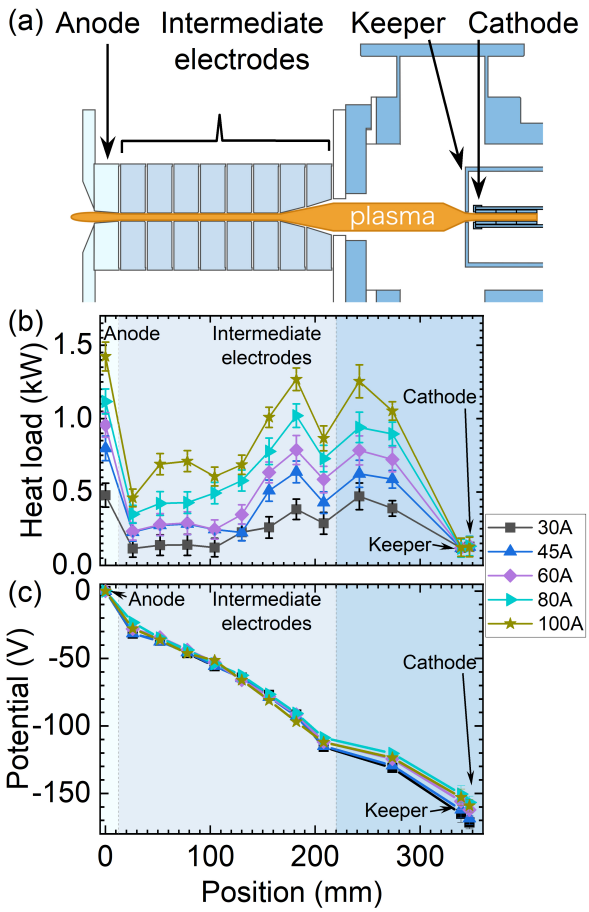

FIG. 7. (a) Schematic diagram of the electrodes (b) the heat load on each electrode and (c) the electric potential profile along the channel.

order smaller than the observed heat load. This means that the plasma parameter abruptly changed at the anode. The abrupt change of the plasma parameter around the anode has been documented by Van de Sanden, where the shock structure just at the anode exit of the cascade arc discharge was observed using the Thomson and Rayleigh scattering measurement[32]. In this case, the temperature and density of the neutral, ion, and electron abruptly drops within a few centimeters from the anode, which is consistent with the Mott-Smith relation[33]. Figure 8 shows the dependence of the electron density evaluated from the H-β Stark broadening analysis on the discharge power at a gas flow rate of 0.54 L/min. The electron densities at the anode and cathode are increased with the discharge power. The electron density reaches 1.1×10^{20} m^{-3} at a discharge power of 15 kW.

Figure 9 (a) and (b) show the dependence of the electron density and temperature at 2 cm downstream from the keeper electrode observed by the Thomson scattering measurement, respectively, on the discharge power. The electron temperature, T_e, is found to be irrelevant to the discharge power and the gas flow rate. On the other hand, the electron density, n_e, in the vicinity of the keeper electrode is increased with the

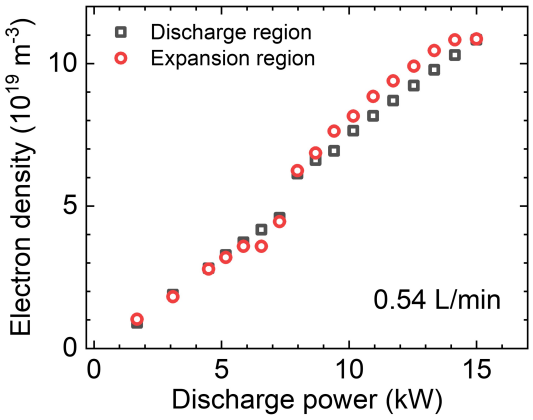

FIG. 8. Electron density determined from the H-β Stark broadening at cathode and anode. The observation is performed at a gas flow rate of 0.54 L/min.

discharge power, which is consistent with the result obtained by the H-β Stark broadening.

We performed the power balance analysis of the electron thermal energy to estimate the neutral gas temperature, T_n, and density, n_n, inside the channel by assuming a stationary condition. The power balance analysis of the electron thermal energy has been applied to obtain the gas temperature, T_n, between the anode and cathode of the steady-state high-pressure arc discharge[31]. In the case of high-pressure arc discharge, the power balance analysis takes into account the electron heating by the electric field and the energy loss by collision with the ions as follows:

$$\frac{3}{2}\kappa\frac{\partial T_e}{\partial t} = \frac{e^2E^2}{m_e\nu_{ei}} - \frac{3}{2}\nu_{E_{ei}}\kappa(T_e - T_i). \quad (1)$$

Here, $\kappa, T_i, e, E, m_e, \nu_{ei}$, and $\nu_{E_{ei}}$ represent the Boltzmann constant, ion temperature, element charge, electric field, electron mass, collision frequency between electron and ion, and energy relaxation frequency of electron when considering the collision with the ions, respectively. The ion temperature is estimated by finding the T_i where right hand side (RHS) of Eq. (1) become zero. In the case of the cascade arc discharge, on the other hand, the neutral density, n_n, is expected to be high and the electrode wall limits the plasma boundary, so that the energy loss by excitation and ionization as well as the thermal transport in the radial direction cannot be neglected. In addition to the radial variation of the plasma parameters, the divergence of the heat flux along the channel must be taken into account, since the electron density is expected to vary along the channel, as expected from the emission intensity variation in Fig. 4(a), and there exists a strong axial flow of electrons inside the channel. Therefore, the power balance analysis must include the above-mentioned terms to estimate

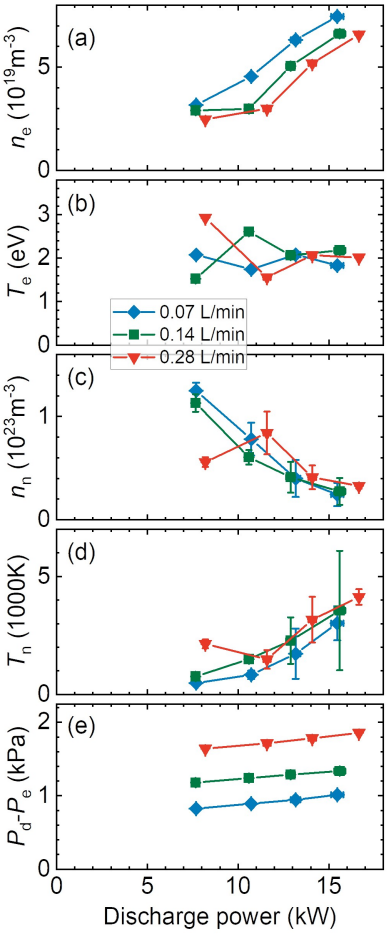

FIG. 9. (a)(b) Electron density (n_e) and temperature (T_e) at cathode exit observed by the Thomson scattering measurement, respectively. (c)(d) Neutral density (n_n) and temperature (T_n) at cathode exit estimated from the power balance analysis, respectively. (e) The pressure difference between gas inlet (P_d) and vacuum vessel (P_e).

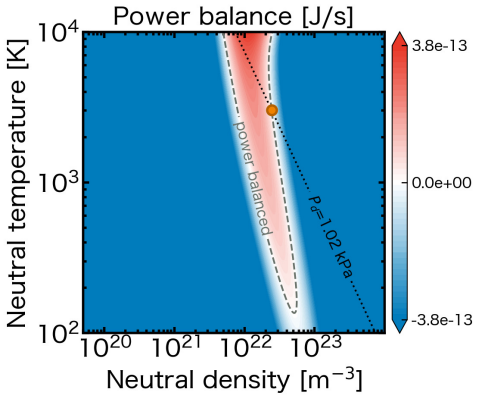

FIG. 10. The dependence of RHS of Eq. (2) on the neutral density and temperature when the gas flow rate was 0.07 L/min and discharge power was 16 kW. The black dashed line indicates the condition where the RHS is zero. The dotted line shows the condition where $n_n\kappa T_n = P_d$ (in this case P_d= 1.02 kPa) is satisfied.

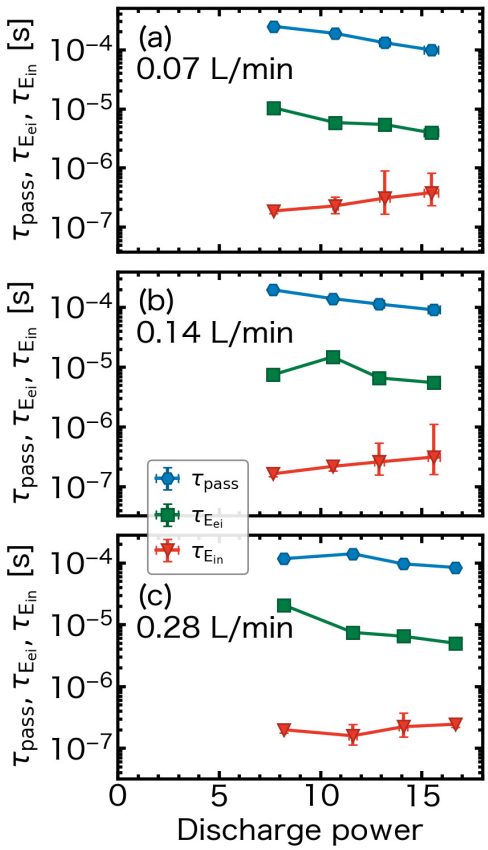

FIG. 11. Comparison of the time of the neutral particles pass through the channel, energy transfer time between electron and neutral, and that between ion and neutral for the gas flow rates of (a) 0.07 L/min (b) 0.14 L/min and (c) 0.28 L/min.

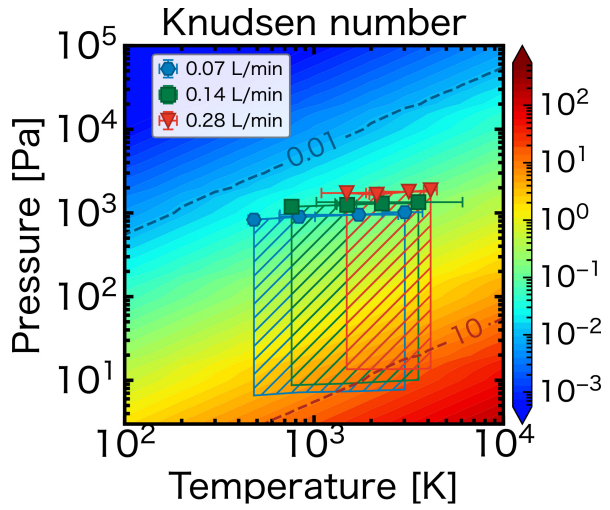

FIG. 12. The Knudsen number as a function of gas temperature and pressure. The contour lines denoting Kn=0.01 and Kn=10 represent the boundary for continuum flow and molecular flow, respectively. The points represent the Knudsen number at the cathode exit and the hatched region represent the range of Knudsen number inside the channel. The lower boundary of the hatched region represent the pressure in the vacuum vessel for each condition.

the neutral temperature, T_n, and density, n_n, as follow:

$$\frac{3}{2}\kappa\frac{\partial T_e}{\partial t} = \frac{e^2E^2}{m_e(\nu_{ei}+\nu_{en})} - \frac{3}{2}\left(\nu_{E_{ei}}+\nu_{E_{en}}\right)\kappa(T_e-T_i) - \frac{1}{n_e}E_{exci.}\langle\sigma_{exci.}v_e\rangle n_n - \frac{1}{n_e}E_{ion.}\langle\sigma_{ion.}v_e\rangle n_n - \frac{1}{n_e}\frac{\partial}{\partial r}\left(\kappa T_e D_{de}\frac{\partial n_e}{\partial r}\right) - \frac{1}{n_e}\frac{\partial}{\partial z}\left(\bar{\nu}_{ze}n_e\kappa T_e\right). \quad (2)$$

Here, $\nu_{en}, \nu_{E_{en}}, E_{exci.}, E_{ion.}, \sigma_{exci.}, \sigma_{ion.}, D_{de}$ and $\bar{\nu}_{ze}$ represent the electron-neutral collision frequency, the energy relaxation frequency of electrons when considering the electron-neutral collision, excitation and ionization energy, excitation and ionization cross section, the dielectric diffusion coefficient, and the mean electron flow along the channel, respectively. The bracket $\langle\rangle$ corresponds to the rate coefficient for relevant atomic process. Typical cross sections of the single atom are adopted for the calculation of the second term on the RHS of Eq. (2), namely, electron-neutral collision cross section of $\sigma_{en} = 0.75\times10^{-20}$ m^2 and ion-neutral collision cross section of $\sigma_{in} = 3.0\times10^{-20}$ m^2. The excitation and ionization energy and cross section for these reactions are referenced from NIST database[34] and Ref.[35]. The discharge was initiated by applying the axial magnetic field strength of 30 mT at the cathode exit, resulting in the electron and ion gyro radius of 0.1 mm and 4-6 mm, respectively. The electron and ion gyro frequency, the electron-ion and ion-neutral collision frequency around the cathode tip are about 0.83 GHz, 114 kHz, 2.9 GHz, and 12 MHz, respectively, and thus the electrons and ions are not magnetized just at the downstream of the cathode and the assumption of dielectric diffusion is expected to dominate the process of radial diffusion of thermal energy. The dielectric diffusion coefficient D_{de} can be written as follows:

$$D_{de} = \mu_i\left(\frac{\kappa T_e}{e}+\frac{\kappa T_i}{e}\right) = \frac{e}{\sigma_{in}n_n\sqrt{\kappa m_i T_i}}\left(\frac{\kappa T_e}{e}+\frac{\kappa T_i}{e}\right). \quad (3)$$

As for the divergence of the heat flux along the channel, it is reported in some literature on the hollow cathode[20,21,36] that the density takes its maximum at the orifice (the exit of the hollow cathode) and decreases along the axis, while the electron temperature does not significantly change. Therefore, the heat flux at the exit of the hollow cathode is expected to contribute to heating. The mean electron flow along the channel $\bar{\nu}_{ze}$ is calculated from the electron mobility as follows:

$$\bar{\nu}_{ze} = \frac{eE}{m_e\nu_{ei}}. \quad (4)$$

The length of the bright region shown in Fig. 4(a) and the radius of the channel are adopted as the scale length of the gradient of plasma parameter in the axial and radial direction, namely 50 mm and 4 mm, respectively, to compute the axial heat flux and dielectric diffusion component. Using the above-mentioned conditions and assuming that the ion and neutral have the same temperature, $T_i = T_n$, the neutral temperature and density are estimated by finding these parameters

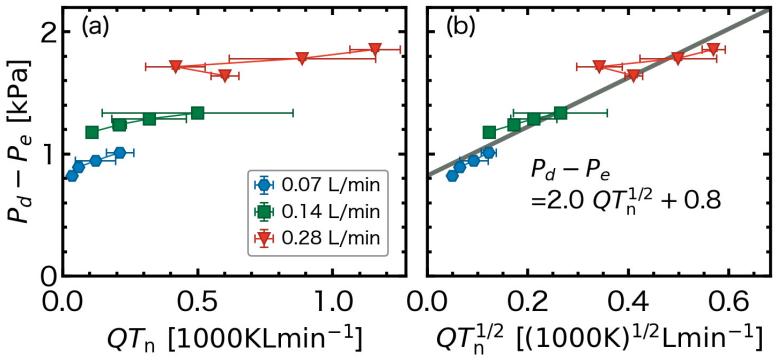

FIG. 13. The dependence of the pressure difference on (a) QT_{n} and (b) $QT_{\mathrm{n}}^{\frac{1}{2}}$.

where RHS of Eq. (2) is balanced, and the equation-of-state for the ideal gas $n_{\mathrm{n}}\kappa T_{\mathrm{n}} = P_{\mathrm{d}}$ is fulfilled. The electric field is calculated from the electrode potential profile, and the electron temperature and density are determined by the Thomson scattering measurement.

Figure 10 shows the dependence of the RHS of Eq. (2) on the neutral temperature and density when the gas flow rate is 0.07 L/min and the discharge power is 16 kW. The dashed and the dotted line represent the condition where RHS of Eq. (2) is balanced and the equation-of-state for the ideal gas is satisfied, respectively. The intersection of the dashed and dotted lines denoted by the orange dot is adopted as the estimated neutral temperature and density. The dependence of the estimated neutral temperature and density on the discharge power are shown in Fig. 9 (c) and (d), respectively, indicating that the neutral temperature is increased up to 4000 K, and the neutral density is decreased with increasing the discharge power. The decrease in the neutral density with increasing the discharge power suggests that the gas flow velocity increases with the discharge power, which is consistent with the increase in the neutral temperature. Also, Fig. 9 (e) suggests that the pressure difference sustained by the PW increase with the increase in the neutral temperature.

The validity of the estimated neutral density is confirmed by calculating the equilibrium of the ionization and the recombination process, $n_{\mathrm{e}}\langle\sigma_{ion.}v_{\mathrm{e}}\rangle n_{\mathrm{n}} = n_{\mathrm{e}}\alpha(T_{\mathrm{e}})n_{\mathrm{i}}$, where $\alpha(T_{\mathrm{e}})$ represents the rate coefficient of the radiative recombination. Since the rate coefficient of the ionization is in the order of 10^{-21} m^{3}s^{-1} and typical rate coefficient of the radiative recombination for $T_{\mathrm{e}}\sim$ 2.0 eV and $n_{\mathrm{e}} \sim 10^{19}$ m^{-3} is 10^{-19} m^{3}s^{-1} [37], the neutral density must be two to three order of magnitude higher than the electron and ion density, which is consistent with the estimated neutral density and observed electron density. Therefore, the estimated neutral temperature and density and their dependence on the discharge power are consistent with the other restrictions, implying the validity of the estimation.

The particle traveling time in the channel, electron-ion and ion-neutral energy relaxation time are compared to validate the assumption of $T_{\mathrm{i}} = T_{\mathrm{n}}$ and to check whether the ions and neutrals can acquire energy from the electrons. Figure 11 indicates that the particle passing time τ_{pass} is 1-3 orders of magnitude longer than the electron-ion and ion-neutral energy relaxation time , $\tau_{\mathrm{E_{ei}}}$ and $\tau_{\mathrm{E_{in}}}$, for present experimental conditions. This result shows that the neutral particles have time enough to exchange the energy of the plasma, indicating that the cascade arc apparatus has sufficient ability to heats the neutral gas to improve the pressure separation capability significantly.

C. Conductance characteristics

A conductance represents the flow rate through a channel for a unit difference in pressure between the inlet and outlet of the channel, namely,

$$Q = C\,\Delta P. \tag{5}$$

Here $Q, C,$ and ΔP represent the flow rate, conductance, and the pressure difference between the inlet and outlet of the channel, respectively. The Eq. 5 reads that a higher flow rate is expected as the conductance is increased. On the other hand, a PW is designed to sustain a higher pressure difference between the inlet and outlet of the channel, $\Delta P = P_{\mathrm{d}} - P_{\mathrm{e}}$, so the conductance of the channel must be reduced to enhance the performance of PW. Therefore, in this section, we consider the relation between the pressure difference and the flow rate using the inverse of the conductance $U = 1/C$ as follows,

$$P_{\mathrm{d}} - P_{\mathrm{e}} = U(T_n)\,Q. \tag{6}$$

Here, the inverse of the conductance is described as a function of gas temperature, as can be seen from the discussion below.

The conductance characteristics were analyzed using the observed pressure and estimated neutral density and temperature. Figure 12 shows the Knudsen number of the neutral gas inside the channel. A fluid is classified as continuum flow, molecular flow and intermediate flow when the Knudsen number is in the range of $Kn < 0.01, Kn > 10$, and $0.01 \leq Kn \leq 10$, respectively. Since the dependence of the conductance on the gas temperature differs with the class of the fluids, the pressure separation capability could change with the condition of the fluid inside the channel. The conductance characteristics of the viscous continuum flow ($Kn < 0.01$) can be described

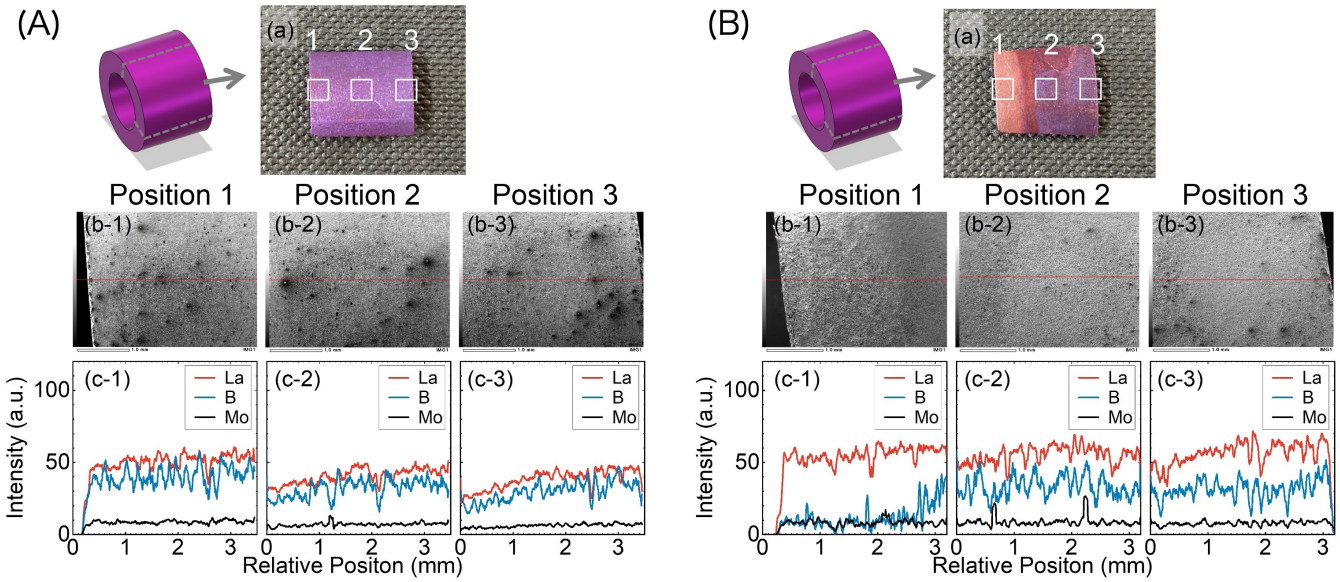

FIG. 14. (A) (a) Schematic view of the LaB_6 cathode and the photograph of the outer surface of the LaB_6 cathode before discharge. (b1-3) The SEM image of the outer surface of LaB_6 . (c1-3) The intensity profile of lanthanum, boron and molybdenum at the midplane of the SEM image (c1-3) before discharge. (B) (a) Schematic view of the LaB_6 cathode and the photograph of the outer surface of the LaB_6 cathode after discharge. (b1-3) The SEM image of the outer surface of LaB_6 . (c1-3) The intensity profile of lanthanum, boron and molybdenum at the midplane of the SEM image (c1-3) after discharge.

by the Hagen-Poiseuille equation as follows[38]:

$$P_{\mathrm{d}} - P_{\mathrm{e}} = \frac{\mu l}{4\pi d^4} Q, \tag{7}$$

where $d, l,$ and μ represent the channel diameter, its length and the gas viscosity, respectively. Thus, the pressure separation capability of a PW is proportional to the viscosity and gas flow rate when the Knudsen number is sufficiently small. Theoretical study has revealed that the viscosity of the He gas is increased almost linearly for the gas temperature up to 17000 K [39], resulting in the relation $\mu \propto T_n$. These results indicates that the pressure difference $P_{\mathrm{d}} - P_{\mathrm{e}}$ is proportionally increased with the gas temperature if the fluid inside the channel can be regarded as viscous continuum flow. On the other hand, the conductance of the molecular flow (Kn>10) can be described as follows[40]:

$$P_{\mathrm{d}} - P_{\mathrm{e}} = \frac{3}{8\pi} \sqrt{\frac{\kappa T_{\mathrm{n}}}{2\pi m_{\mathrm{n}}}} Q. \tag{8}$$

Thus, the pressure separation capability is proportional to $\sqrt{T_{\mathrm{n}}}$ when the fluid inside the channel is regarded as molecular flow. Figure 12 shows that the gas flowing inside the channel of the large-bore PW lies in the domain of the molecular flow or intermediate flow[29]. Figure 13 describes the dependence of the pressure difference $P_{\mathrm{d}} - P_{\mathrm{e}}$ on the gas flow rate and temperature. Figure 13 (b) shows that the pressure difference is proportional to $QT_{\mathrm{n}}^{\frac{1}{2}}$, not to QT_{n} as shown in Fig. 13 (a), and thus the gas flow of the large-bore PW is classified as a molecular flow. These findings emphasize the importance of the gas temperature to improve the pressure separation capability of the large-bore PW.

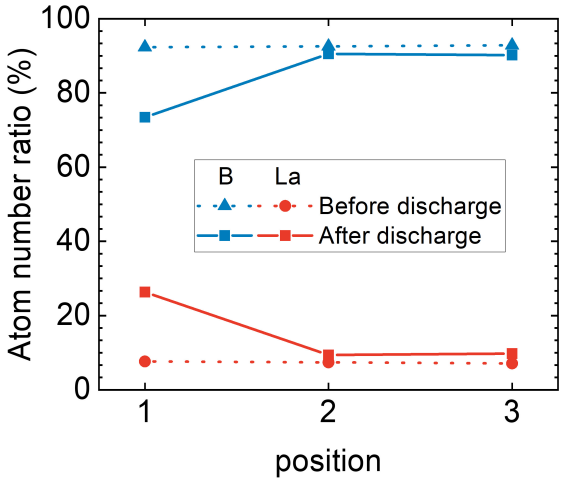

FIG. 15. Atom number ratio at the outer surface of LaB_6 before and after discharge. The EDX intensity at 0.18 and 4.6 keV are used for calculating the atom number ratio of boron and lanthanum, respectively.

D. Cathode material features

Figure 14 (A-a) and (B-a) show the photograph and SEM (Scanning Electron Microscopy) image of the LaB_6 cathode before and after more than 10 hours exposure to the discharge, respectively. We can see from Fig. 14 (A-a) and (B-a) that the color of the part of the LaB_6 cathode surface change from deep purple to red purple. The EDX (Energy Dispersive X-

ray) analysis shows the decrease in the intensity of the spectrum from the boron in the region where the color of the LaB_6 changed to red purple (see Fig. 14 (A-b,c) and (B-b,c)). The detailed EDX analysis within the whole region of interest shows that the ratio of the number of boron decreased by 20 % after discharge at the same region, as shown in Fig. 15. It is reported that the color of the LaB_6 change to red purple when the atom number ratio of boron is decreased[20,41]. In addition, the study on the boride cathodes has shown that the boron diffuses to the lattice defect of molybdenum when the attached LaB_6 and molybdenum are heated[23]. Cracks are also observed on the molybdenum shaft after more than 50 hours of discharge exposure, and white powder is produced from the LaB_6 cathode surface, which are the indication of the migration of boron atoms to the molybdenum as reported in Ref. [20,42]. These results and previous studies show that the boron diffused to the molybdenum shaft during the discharge and other material or structures must be adopted to the cathode shaft for realizing long operation duration of the PW, such as buffer material between LaB_6 and molybdenum or fabrication of the shaft with carbon.

IV. SUMMARY

We have developed a cascade arc discharge apparatus for an 8-mm large bore PW equipped with an indirectly heated hollow cathode to realize sufficiently high-pressure separation capacity and long duration for paving the way for a broader range of the application of the quantum beam science. The developed PW successfully separated 2.4 kPa and 16 Pa, and pressure separation capability was sustained for more than 1 hour. H-β Stark broadening and the Thomson scattering measurements showed that the electron density and temperature inside reached 10^{19}-10^{20} m^{-3} and 2.0 eV, respectively, indicating that high-density and high-temperature plasma was produced in the channel. The power balance analysis on the electron thermal energy revealed that the neutral density and temperature inside the channel reached 10^{23} m^{-3} and 4000 K, respectively. The conductance analysis confirmed that the gas temperature, thus the electron temperature and density, is an important parameter to improve the pressure separation capability of the large-bore PWs. The SEM-EDX analysis on the LaB_6 cathode showed that the boron diffused to the molybdenum shaft. The molybdenum shaft became brittle after more than 50 hours of discharge, indicating that the replacement of buffer material from molybdenum to other material is necessary for long-duration operation.

ACKNOWLEDGEMENT

This research was supported by JSPS KAKENHI under Grant No. JP20H00141, O. S. G. Fund, Furukawa research fund, and NIFS Collaboration Research Program under Grant No. NIFS NIFS22KIIH003, NIFS22KIIH011, and NIFS23KIIH016.

DATA AVAILABILITY

The data that support the findings of this study are available from the corresponding author upon reasonable request.

REFERENCES

[1] A. Hershcovitch, "A plasma window for transmission of particle beams and radiation from vacuum to atmosphere for various applications," Physics of Plasmas **5**, 2130–2136 (1998).
[2] S. Huang, K. Zhu, Y. R. Lu, S. Z. Wang, A. Hershcovitch, L. Yang, and X. Y. Zhang, "Quantitative characterization of arc discharge as vacuum interface," Physics of Plasmas **21**, 123511 (2014).
[3] S. Namba, Y. Iwamoto, Y. Asano, T. Shugyo, K. Fukuyama, N. Ikoma, H. Okuno, N. Tamura, and T. Endo, "High-density cascade arc plasma sources for application to plasma windows for virtual vacuum interfaces," Physics of Plasmas **25** (2018), 10.1063/1.5070071/263262.
[4] A. Hershcovitch, "High-pressure arcs as vacuum-atmosphere interface and plasma lens for nonvacuum electron beam welding machines, electron beam melting, and nonvacuum ion material modification," Journal of Applied Physics **78**, 5283–5288 (1995).
[5] B. T. Pinkoski, I. Zacharia, A. Hershcovitch, E. D. Johnson, and D. P. Siddons, "X-ray transmission through a plasma window," Review of Scientific Instruments **72**, 1677–1679 (2001).
[6] W. A. J. Vijvers, D. C. Schram, A. E. Shumack, N. J. Lopes Cardozo, J. Rapp, and G. J. van Rooij, "Experimental and theoretical determination of the efficiency of a sub-atmospheric flowing high power cascaded arc hydrogen plasma source," Plasma Sources Science and Technology **19**, 065016 (2010).
[7] N. Ikoma, Y. Miyake, M. Takahashi, H. Okuno, S. Namba, K. Takahashi, T. Sasaki, and T. Kikuchi, "Demonstration of Plasma Window with 20 mm Diameter and Pressure Separation for Accelerator Applications," Plasma and Fusion Research **14**, 1206148–1206148 (2019).
[8] X. Yu, X. Yang, C. Xiao, M. Xu, R. He, T. Xu, Y. Ge, Z. Zhang, M. Wu, Y. Yu, K. Zhu, and X. Wang, "Experimental studies of a novel one-dimensional plasma window," Physics of Plasmas **29**, 093509 (2022).
[9] F. Marti, "HEAVY ION STRIPPERS," Proceedings of LINAC2012 , 1050–1054 (2012).
[10] T. Maruta, Y. Yamazaki, H. Ao, S. Beher, G. Bollen, N. Bultman, F. Casagrande, S. Cogan, C. Compton, J. Curtin, K. Davidson, K. Dixon, K. Elliott, A. Facco, V. Ganni, A. Ganshyn, J. Gao, P. Gibson, T. Glasmacher, Y. Hao, M. Hausmann, L. Hodges, K. Holland, K. Hosoyama, H.-C. Hseuh, M. Ikegami, S. Jones, T. Kanemura, M. Kelly, M. Larmann, R. E. Laxdal, J. Letourneau, S. Lidia, G. Machicoane, F. Marti, P. Manwiller, S. Miller, Y. Momozaki, D. Morris, P. Ostroumov, J. Popielarski, L. Popielarski, J. Priller, H. Ren, K. Saito, A. Stolz, X. Wang, J. Wei, M. Wiseman, T. Xu, Q. Zhao, and S. Zhao, "FRIB," **17**, 269–278 (2021).
[11] H. Imao, H. Okuno, H. Kuboki, S. Yokouchi, N. Fukunishi, O. Kamigaito, H. Hasebe, T. Watanabe, Y. Watanabe, M. Kase, and Y. Yano, "Charge stripping of U238 ion beam by helium gas stripper," Physical Review Special Topics - Accelerators and Beams **15**, 123501 (2012).
[12] H. Imao, H. Okuno, and H. Kuboki, "DEVELOPMENT OF GAS CHARGE STRIPPER FOR INTENSE HEAVY ION BEAM," Proceedings of the 10th Annual Meeting of Particle Accelerator Society of Japan , 294–298 (2013).
[13] A. L. LaJoie, Viability and characterization of a plasma window as a flow limiter for an ion Ph.D. thesis, Michigan State University (2020).
[14] J. L. Delcroix and A. R. Trindade, "Hollow Cathode Arcs," Advances in Electronics and Electron Physics **35**, 87–190 (1974).
[15] B. E. Keen and R. V. Aldridge, "Low frequency wave mixing in a magneto-plasma," Physics Letters A **29**, 225–226 (1969).
[16] D. A. Huchital and J. D. Rigden, "Functional Ion Laser Based upon a Thermionic Hollow Cathode Discharge," Review of Scientific Instruments **39**, 1472–1477 (1968).
[17] W. C. Jennings, J. H. Noon, E. H. Holt, and R. G. Buser, "Comparison of Hollow Cathode and Conventional Argon Ion Lasers," Review of Scientific Instruments **41**, 322–326 (1970).
[18] D. M. Goebel and E. Chu, "High-Current Lanthanum Hexaboride Hollow Cathode for High-Power Hall Thrusters," https://doi.org/10.2514/1.B34870 **30**, 35–40 (2014).
[19] M. A. Silva, A. E. Martinelli, C. Alves, R. M. Nascimento, M. P. Távora, and C. D. Vilar, "Surface modification of Ti implants by plasma oxidation

in hollow cathode discharge," Surface and Coatings Technology **200**, 2618–2626 (2006).
[20]D. M. Goebel and R. M. Watkins, "Compact lanthanum hexaboride hollow cathode," Review of Scientific Instruments **81** (2010), 10.1063/1.3474921/351540.
[21]G. Becatti, D. M. Goebel, J. E. Polk, and P. Guerrero, "Life Evaluation of a Lanthanum Hexaboride Hollow Cathode for High-Power Hall Thruster," https://doi.org/10.2514/1.B36659 **34**, 893–900 (2017).
[22]D. M. Goebel, J. T. Crow, and A. T. Forrester, "Lanthanum hexaboride hollow cathode for dense plasma production," Review of Scientific Instruments **49**, 469–472 (1978).
[23]J. M. Lafferty, "Boride Cathodes," Journal of Applied Physics **22**, 299–309 (1951).
[24]M. A. Gigosos, M. González, and V. Cardeñoso, "Computer simulated Balmer-alpha, -beta and -gamma Stark line profiles for non-equilibrium plasmas diagnostics," Spectrochimica Acta Part B: Atomic Spectroscopy **58**, 1489–1504 (2003).
[25]Kevin Finch, Aldo Hernandez, Yue She, Songyue Shi, and Gerardo Gamez, "A transmission-type triple grating spectrograph for improved laser scattering diagnostics of low-density plasmas used in chemical analysis," Journal of Analytical Atomic Spectrometry **35**, 1932–1946 (2020).
[26]M. Kaloyan, S. Ghazaryan, S. P. Tripathi, W. Gekelman, M. J. Valle, B. Seo, and C. Niemann, "First Results from the Thomson Scattering Diagnostic on the Large Plasma Device," Instruments 2022, Vol. 6, Page 17 **6**, 17 (2022).
[27]N. Yamamoto, K. Tomita, K. Sugita, T. Kurita, H. Nakashima, and K. Uchino, "Measurement of xenon plasma properties in an ion thruster using laser Thomson scattering technique," Review of Scientific Instruments **83**, 73106 (2012).
[28]K. Tomita, Y. Sato, N. Bolouki, T. Shiraishi, K. Uchino, Y. Miwa, T. Kobayashi, and S. Inagaki, "Measurement of Electron Density and Temperature Using Laser Thomson Scattering in PANTA," Plasma and Fusion Research **12**, 1401018–1401018 (2017).
[29]K. Yamasaki, O. Yanagi, Y. Sunada, K. Hatta, R. Shigesada, M. Sumino, T. Yamaguchi, M. Islam, N. Tamura, H. Okuno, and S. Namba, "Discharge characteristics of steady-state high-density plasma source based on cascade arc discharge with hollow cathode," Review of Scientific Instruments **93** (2022), 10.1063/5.0076388.
[30]S. Namba, T. Shikama, W. Sasano, N. Tamura, and T. Endo, "Characteristics of an under-expanded supersonic flow in arcjet plasmas," Japanese Journal of Applied Physics **57**, 066101 (2018).
[31]Y. P. Raizer, Gas discharge physics (Springer, 1997) p. 449.
[32]M. C. M. V. d. Sanden, J. M. d. Regt, and D. C. Schram, "The behaviour of heavy particles in the expanding plasma jet in argon," Plasma Sources Science and Technology **3**, 501–510 (1994).
[33]H. M. Mott-Smith, "The Solution of the Boltzmann Equation for a Shock Wave," Physical Review **82**, 885–892 (1951).
[34]"Atomic Spectra Database | NIST," 10.18434/T4W30F.
[35]Y. Ralchenko, R. K. Janev, T. Kato, D. V. Fursa, I. Bray, and F. J. de Heer, "Electron-impact excitation and ionization cross sections for ground state and excited helium atoms," Atomic Data and Nuclear Data Tables **94**, 603–622 (2008).
[36]D. M. Goebel, K. K. Jameson, R. M. Watkins, I. Katz, and I. G. Mikellides, "Hollow cathode theory and experiment. I. Plasma characterization using fast miniature scanning probes," Journal of Applied Physics **98**, 113302 (2005).
[37]E. Hinnov and J. G. Hirschberg, "Electron-Ion Recombination in Dense Plasmas," Physical Review **125**, 795–801 (1962).
[38]L. D. Landau and E. M. Lifshitz, Fluid Mechanics, 6th ed. (Butterworth-Heinemann, 1987).
[39]S. Janisson, A. Vardelle, J. Coudert, E. Meillot, B. Pateyron, and P. Fauchais, "Plasma Spraying Using Ar-He-H₂ Gas Mixtures," Journal of Thermal Spray Technology **8**, 545–552 (1999).
[40]W. Steckelmacher, "A review of the molecular flow conductance for systems of tubes and components and the measurement of pumping speed," Vacuum **16**, 561–584 (1966).
[41]P. P. Guerrero Vela, J. E. Polk, M. H. Richter, and A. Lopez Ortega, "Dynamic thermal behavior of polycrystalline LaB ₆ hollow cathodes," Journal of Applied Physics **130**, 083303 (2021).
[42]H. N. Olsen, "Thermal and Electrical Properties of an Argon Plasma," Physics of Fluids **2**, 614 (1959).